ACS APPLIED MATERIALS & INTERFACES

Research Article

www.acsami.org

Three-Dimensional Ni/SnO_x/C Hybrid Nanostructured Arrays for Lithium-Ion Microbattery Anodes with Enhanced Areal Capacity

Jianhui Zhu,* Jian Jiang, Yamin Feng, Gaoxiang Meng, Hao Ding, and Xintang Huang*

Institute of Nanoscience and Nanotechnology, Central China Normal University, Wuhan 430079, P. R. China

Supporting Information

ABSTRACT: The areal capacity of lithium-ion microbatteies (LIMBs) can be potentially increased by adopting a three-dimensional (3D) architectured electrode. Herein, we report the novel 3D Ni/SnO_x/C hybrid nanostructured arrays that were built directly on current collectors via a facile hydrothermal method followed by a calcination-reduction process. Branched SnO_2 nanorods grew uniformly on $Ni_2(OH)_2CO_3$ nanowall arrays, resulting in the formation of precursors with a 3D interconnected architecture. By using ethylene glycol as the reducing agent, the glucose-coated $SnO_2/Ni_2(OH)_2CO_3$ precursors were evolved into an interesting 3D Ni/SnO_x/C hybrid nanostructured arrays within the calcination treatment. Compared to conventional 2D SnO_x/C nanorod arrays, the electrode of 3D Ni/SnO_x/C hybrid nanostructured arrays exhibited enhanced lithium storage capacity per unit area, preferable rate capability and improved cycling performance when tested for LIMBs. The superior performance might be attributed to the open-up Ni frameworks that can not only serve as effective channels for electrons transport and Li^+ diffusion but also help to accommodate the large volume changes upon lithiation/delithiation.

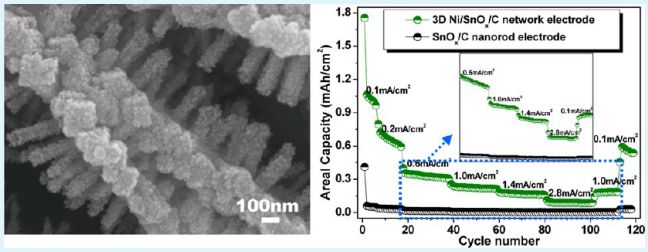

KEYWORDS: *three-dimensional, Ni/SnO_x/C nanostructured arrays, lithium-ion microbatteries, anode, enhanced areal capacity*

INTRODUCTION

With rapid advances in the fields of microelectronics, such as microsensors, micromachines and drug delivery systems, etc., it is of great importance to develop integrated power sources that enable the continued device operation when the electrical plug-in is not available.[1−3] To meet these demanding applications, lithium-ion microbatteries (LIMBs) with higher energy and power density per unit area are urgently required.[4,5] To date, many approaches have been tried to upgrade the LIMBs performance. Among strategies, one smart and effective way to increase the areal capacity is to use the three-dimensional (3D) architectured hybrid nanostructured arrays.[6−8] Compared to conventional planar two-dimensional (2D) designs, nanostructured arrays with a 3D configuration can exhibit special advantages for LIMBs: (I) The 3D hybrid architectured designs can make the areal capacity of electrodes enhanced because of the increased mass loading of active materials per unit area; (II) The open-up interconnected Ni networks in 3D nanostructured arrays can provide both electronic and ionic pathways, allowing for the efficient charge transfer and mass exchanges during the repeated charge/discharge processes; (III) There exists a large amount of space available in 3D nanostructured arrays, which is helpful to accommodate volume changes caused by Li^+ insertion/extraction.[9,10] Several 3D configurations have been proposed for LIMBs recently.[11−14] Normally, these 3D structures have been realized mainly by the standard physical/chemical deposition of active material layers onto a sort of conductive matrixes made by the inverse opal structures, coaxial nanostructures, mesoporous materials, or metal foam systems.[11−14] However, when taking into account cost, complexity, and other fabrication issues, there is still a lack of a simple and economic strategy to construct the 3D architectured electrodes.

In addition to electrode architectures, searching for suitable high-capacity electrode materials (at least higher than commercial graphite materials in capacity) to couple with such 3D configurations is also important and highly required to achieve high-performance LIMBs.[7,15] Sn-based materials have long been regarded as one of most promising candidates for next-generation anode materials because of their high specific capacity and good environmental benignity. Sn, a member of the alloy-type anode materials, shows excellent electrochemical lithium alloying capabilities that as much as 4.4 Li^+ ions can insert into one Sn atom to form $Li_{4.4}Sn$ alloys, corresponding to a theoretical specific capacity of 994 mA h/g.[16] Besides, its oxide SnO_2 can also store over twice as much lithium as the conventional graphite (372 mA h/g); therefore, a theoretical specific capacity of about 781 mA h/g can be reached.[17−19] Despite their high-capacity properties, Sn-based anode materials have to face a major challenge, that is, the large volume changes accompanying the Li^+ insertion/extraction processes. This volume change leads to severe mechanical

Received: January 7, 2013
Accepted: March 14, 2013
Published: March 14, 2013

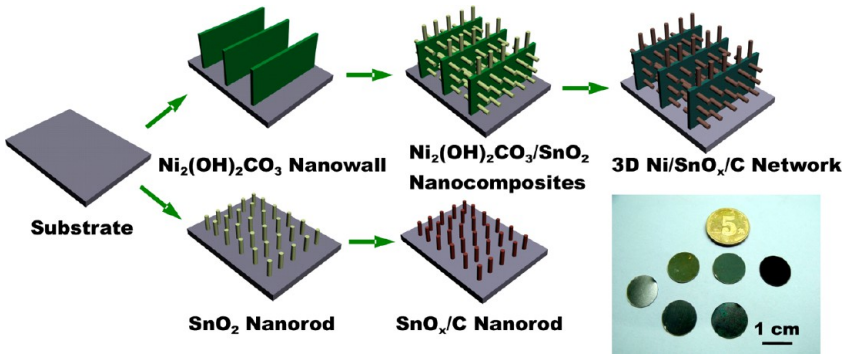

Figure 1. Schematic illustration for the synthetic strategies of the 3D Ni/SnO_x/C network and the SnO_x/C nanorod. Inset is a photograph that displays the corresponding evolution products.

strains that severely limit the electrode cycling life.[16−20] One possible way to address this issue is the structural modification of Sn-based materials on nanoscale in that the electrochemical performance of Sn-based materials seems to have a strong correlation to their structural features.[19−22] Moreover, to make high-performance LIMBs, carbon needs to serve as a significant functional component since it proves to be a good conducting agent and excellent buffer material that can well-prolong the cycling life of electrodes and stabilize their charge−discharge behaviors.[23]

Herein, for the first time, we proposed a novel strategy for the fabrication of 3D Ni/SnO_x/C hybrid nanostructured arrays via a facile hydrothermal method followed by a calcination-reduction treatment. Carbon coated SnO_x nanorods grew uniformly on metallic Ni nanowall networks, forming a desired 3D hierarchical structure. This unique hybrid architecture can (I) increase the loading of active materials as well as the reaction sites for Li^+ insertion/extraction, thus improving the capacity per unit area, (II) maintain a high electrical conductivity of the overall electrode and facilitate the Li^+ transport, (III) accommodate/alleviate volume changes during the charge/discharge processes.[23] When applied as anode for LIMB, the arrayed 3D hybrid electrodes show a specific areal capacity as high as ∼1.75 mA h/cm^2 at current rate of ∼0.1 mA/cm^2, which is about four times higher than that of conventional 2D planar electrode. Even when the current density was increased by 27 times, the electrode is still able to deliver a capacity of ∼0.11 mA h/cm^2 (more than 18 times that of 2D planar electrode charged/discharged at an even lower rate). In addition, the 3D Ni/SnO_x/C hybrid electrode also exhibited better cycling behavior than that of 2D-designed SnO_x/C hybrids, retaining 72% reversible capacity after 100 cycles. These results demonstrate that our designed electrode with a 3D hybrid configuration is more rational and superior to the 2D electrodes for LIMBs.

EXPERIMENTAL SECTION

Synthesis of SnO_2/$Ni_2(OH)_2CO_3$ Network Precursor. $Ni_2(OH)_2CO_3$ nanowall arrays were synthesized beforehand by referring to our previously reported hydrothermal method.[24] The SnO_2/$Ni_2(OH)_2CO_3$ hierarchical structures were prepared using a catalyst/surfactant-free hydrothermal strategy with a slight modification from the previous reports on the preparation of SnO_2 nanorod arrays.[25] In detail, $Ni_2(OH)_2CO_3$ nanowalls grown on stainless substrate (3 × 4 cm^2) was placed into a 100 mL Teflon autoclave containing the $Sn(OH)_6^{2-}$ dilute aqueous solution that was made by dissolving 0.3 g of $SnCl_4{\cdot}5H_2O$ and 0.9 g of NaOH into 50 mL of deionized water. The autoclave was then sealed, placed into an electric oven, and heated at 220 °C for 2 h. After the equipment cooled down, the substrate was fetched out, washed with deionized water several times, and dried in air at 60 °C.

Synthesis of 3D Ni/SnO_x/C Hybrid Nanostructures. The SnO_2/$Ni_2(OH)_2CO_3$ network precursor built on substrate was first immersed into 0.3 M glucose solution at a constant temperature of 60 °C for 5h. Next, the further calcination and reduction treatments were conducted to achieve the phase transition from the glucose-coated SnO_2/$Ni_2(OH)_2CO_3$ network nanostructures to the desired hybrid products of Ni/SnO_x/C. In our synthesis, the thermal decomposition of $Ni_2(OH)_2CO_3$ as well as the reduction of Ni^{2+} into Ni was accomplished in a horizontal, quartz tube-furnace system by one step. The glucose-coated SnO_2/$Ni_2(OH)_2CO_3$ precursors built on stainless substrate were placed in the center of the quartz-tube furnace. Afterward, the reducing agent of ethylene glycol (total volume: 1 mL) was loaded in an alumina boat and placed at the upstream zone of the quartz tube. Before heating, the quartz tube was sealed and flushed with an Ar flow of 200 sccm for 20 min. The system was then heated to 480 °C with a heating rate of 10 °C min^{-1} under a 50 sccm Ar flow and kept at 480 °C for 30 min, followed by a natural cool-down process.

Synthesis of SnO_x/C Hybrid Nanostructures. The SnO_x/C hybrid nanostructures grown on a 2D planar substrate were synthesized by following the same synthesis procedures mentioned above except that the $Ni_2(OH)_2CO_3$-covered substrate was replaced by a pure stainless substrate.

Sample Characterization. Phase structures of the synthesized samples were characterized by powder X-ray diffraction (XRD) on a Bruker D-8 Advance diffractometer using Cu Kα (λ = 1.5418 Å) radiation. Raman spectroscopy patterns were recorded on a Witech CRM200 Raman microscope using a 532 nm excitation wavelength laser. The morphology and crystalline structure analyses were conducted on a JEOL JSM-6700F field emission scanning electron microscope (FE-SEM) and a JEM-2010 transmission electron microscope (TEM) and high-resolution transmission electron microscope (HRTEM). X-ray photoelectron spectroscopy (XPS) measurements were performed on a Perkin-Elmer PHI 5000C ECSA system with Mg Ka irradiation. The mass loading of the active material was carefully weighed on BS 124S Balance (max 120 g; d = 0.1 mg). On average, ∼0.8 mg of SnO_x/C active material is statistically determined per 1 × 1 cm^2 of Ni nanowall networks, whereas there is only ∼0.3 mg of SnO_x/C weighed per 1 × 1 cm^2 planar stainless substrate.

Electrochemical Measurements. Electrochemical measurements were performed by the use of swagelok-type cells. Cells were assembled in an Ar-filled glovebox (Mbraun, Unilab, Germany) by directly using the as-synthesized 3D Ni/SnO_x/C hybrid nanostructured arrays or SnO_x/C hybrid nanorod arrays on substrate (a circular foil with 14 mm diameter) as anode electrodes. The counter and reference electrodes were lithium metal circular foil (0.59 mm thick, 14 mm diameter), and the electrolyte solution was 1 M $LiPF_6$ in ethylene carbonate (EC) and dimethyl carbonate (DEC) (1:1 by volume). The discharge−charge cycling was conducted at room

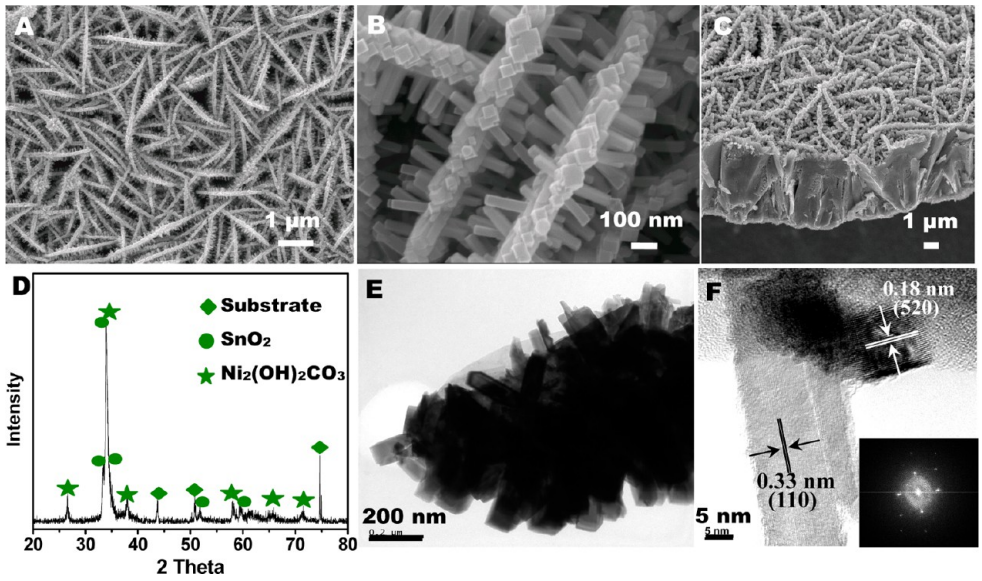

Figure 2. Morphological and structural characterizations of the precursor $Ni_2(OH)_2CO_3/SnO_2$ 3D network arrays: (A, B) typical low- and high-magnification SEM image; (C) cross-sectional SEM image; (D) XRD pattern; (E) TEM image; (F) HRTEM image. Inset in F shows the corresponding SAED pattern.

temperature by using a multichannel battery tester (model SCN, USA). Areal capacity values were calculated based on the area of the working electrode. Cyclic voltammetry (CV) was recorded on the CHI660C electrochemical workstation at a scan rate of 0.5 mV s^{-1}. Electrochemical impedance spectroscopy (EIS) measurements were performed on the electrochemical workstation by applying an AC voltage with 5 mV amplitude in a frequency range from 0.01 Hz to 100 kHz.

RESULTS AND DISSCUSSION

Figure 1 shows the schematic illustration of the synthetic strategy of 3D $Ni/SnO_x/C$ hybrid nanostructured arrays. Typically, for the synthesis of 3D $Ni/SnO_x/C$ hybrids, there are three steps involved during the entire fabrication process: (i) fabrication of $Ni_2(OH)_2CO_3$ nanowall arrays on stainless steel substrate via a hydrothermal method as previously reported by our group,[24] (ii) secondary growth of SnO_2 nanorod branches onto $Ni_2(OH)_2CO_3$ nanowall surface (particularly at the lattices-matched places) along a specific orientation by the slow release of hydroxyl ions and water from $Sn(OH)_6^{2-}$,[21,22a] (iii) coating glucose molecules uniformly on $SnO_2/Ni_2(OH)_2CO_3$ precursors, and then making the intermediate products annealed and reacted with the introduced reducing agent. Compared to former template-assisted ways to build the 3D configurations,[11−14] our method is totally template-free, rather simple. and cost-effective. Besides, we also display the fabrication process of SnO_x/C nanorod arrays, which are obtained by substituting a planar substrate for $Ni_2(OH)_2CO_3$ nanowall arrays. A photograph (inset in Figure 1) successively shows the evolved 3D $Ni/SnO_x/C$ hybrid nanostructured arrays and 2D-designed SnO_x/C nanorod arrays on the substrate.

The evolution of 3D $Ni/SnO_x/C$ hybrid nanostructures has been systematically studied. Figure 2A-C show the scanning electron microscope (SEM) images of $Ni_2(OH)_2CO_3/SnO_2$ precursors. SEM observations reveal that the precursors are composed of interconnected network-like $Ni_2(OH)_2CO_3$ nanowall arrays (Figure 2A), and SnO_2 nanorods (~200 nm in length) uniformly distributed on each nanowall lamella (Figure 2B), leading to the formation of a 3D branched architecture. Figure 2C shows a cross-section SEM image of the hybrid precursors, revealing that the mean thickness of the synthesized $Ni_2(OH)_2CO_3/SnO_2$ nanostructured film is ~5 μm. The crystallographic structure of the phase purity of the $Ni_2(OH)_2CO_3/SnO_2$ precursor were examined by powder X-ray diffraction (XRD), as shown in Figure 2D. Except for peaks from the metal substrate, all diffraction peaks come from the hybrid precursor and match well with the standard XRD patterns of tetragonal SnO_2 (JCPDF: 03−1116) and nullaginite $Ni_2(OH)_2CO_3$ (JCPDF: 35−0501), respectively. Images E and F in Figure 2 display the transmission electron microscope (TEM) observations toward $Ni_2(OH)_2CO_3/SnO_2$ precursors. It is evident that SnO_2 nanorod branches grow robustly on the surface of the single $Ni_2(OH)_2CO_3$ lamella. Moreover, a high-resolution TEM image (Figure 2F) illustrates that the lattice spacing of 0.33 and 0.18 nm, which successively accord well with the (110) and (520) planar space of SnO_2 and $Ni_2(OH)_2CO_3$, are observed at the nanorod-lamella boundary. These results are highly consistent with former SEM observations and XRD analysis, confirming the generated 3D hybrid nanostructures have a $Ni_2(OH)_2CO_3$ nanowalls core and SnO_2 nanorods branches. The Fast Fourier Transform (FFT) pattern (inset in Figure 2F) demonstrates that SnO_2 nanorods possess a single-crystal nature and grow along a preferential direction of [001].

The coating of glucose and the calcination treatment accompanied with a slight reduction process were performed to convert $Ni_2(OH)_2CO_3/SnO_2$ precursors into 3D $Ni/SnO_x/C$ hybrid nanostructured arrays. XRD measurement was used to examine the final products. Corresponding results are shown in Figure 2A. After heating/reduction treatments, there is a strong peak appearing at 44.4°, which can be well-indexed to the (111) facet of Ni (JCPDS no. 04−0850). No signals from $Ni_2(OH)_2CO_3$ or NiO impurity are detected, implying that $Ni_2(OH)_2CO_3$ was completely converted to metallic Ni (JCPDS no. 04−0850). In addition, there are other new diffraction peaks present, corresponding to Sn (JCPDS no. 04−0673) and Ni_3Sn_4 (JCPDS no. 04−0846), respectively. This

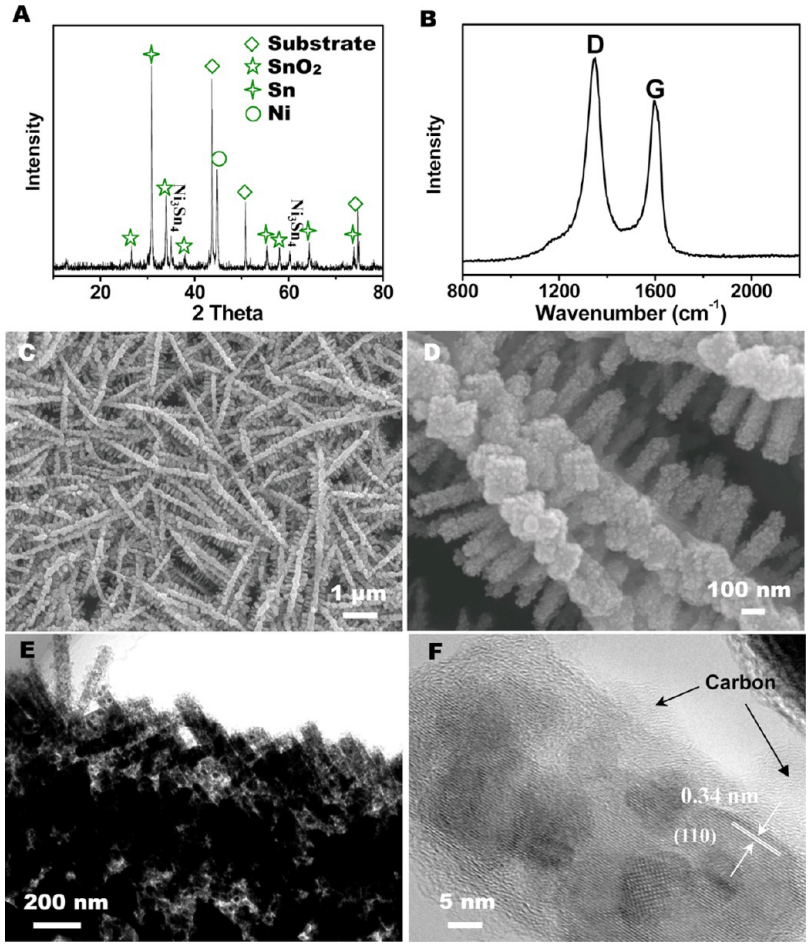

Figure 3. Morphological and structural characterizations of the final product of 3D Ni/SnO_x/C network arrays: (A) XRD pattern; (B) Raman spectrum; (C, D) low- and high-magnification SEM image; (E) TEM image; (F) HRTEM image.

reveals that a portion of SnO_2 was reduced into Sn and moreover little amount of Sn was alloyed with Ni during the calcination process. A Raman spectrum of Ni/SnO_x/C hybrid products has been made in a range of 800−2200 cm^{-1} and displayed in Figure 3B. As observed, two sharp peaks appear at 1349 (D band) and 1595 cm^{-1} (G band), which are the well-known characteristic peaks of carbon materials.[26]

The morphology and structure of final samples were then examined by SEM and TEM. Representative SEM images of Ni/SnO_x/C hybrid products are shown in images C and D in Figure 3. Note that even though suffering from the calcination-reduction process, Ni/SnO_x/C hybrid nanostructured arrays are still able to preserve the geometrical morphology of networklike precursors, without any presence of nanowalls collapse or exfoliation. The top-view SEM image in Figure 3C demonstrates that the formed products own a top-open network structure, wherein a large quantity of void space is dispersed. This can potentially facilitate the ions diffusion and accommodate volume changes upon Li^+ insertion/extraction. The high-resolution SEM image (Figure 3D) shows that SnO_2 nanorods with a smooth structure in precursors have been changed into the rough ones, with nanoparticles distributed on their surface. TEM observations in images E and F in Figure 3 also confirm the generation of rough nanorod structures. From a close observation, it is clear that the nanorods still keep a length of about 200 nm whereas the generated nanoparticles have a diameter of about 20 nm. In the high-resolution TEM image (Figure 3F), the lattice spacing of 0.34 nm is in good agreement with the (001) interplanar spacing of the tetragonal SnO_2, which is well in line with the XRD result. For the comparative study, SnO_2 nanorod arrays (diameter ∼100 nm, height ∼300 nm) grown uniformly on 2D planar substrates were also fabricated (see SEM images in Figure S1B−S1C in the Supporting Information). After the same glucose-coating and calcinations-reduction treatments, the SnO_x/C hybrid nanostructures were made (see SEM images in Figure S2 B, C in the Supporting Information). XRD pattern of this hybrid (see Figure S2A in the Supporting Information) confirms the generation of SnO_2 and Sn, which is quite similar to the case of 3D Ni/SnO_x/C hybrid products. To determine the surface composition and the purity of evolved 3D Ni/SnO_x/C hybrid nanostructured arrays, we performed XPS measurement (see Figure S3 in the Supporting Information). The XPS survey spectrum (see Figure S3A in the Supporting Information) confirms that only Ni, Sn, O, and C elements are detected on the surface of Ni/SnO_x/C hybrids; No other impurities are detected. Figure S3B in the Supporting Information shows the XPS spectrum of Sn 3d, where two prominent peaks are observed at the binding energy of 485.2 eV and 494.6 eV, corresponding to the spin orbit components of Sn $3d_{5/2}$ and Sn $3d_{3/2}$, respectively. This suggests the coexistence of Sn^{4+} and metal Sn in the hybrid products,[27] agreeing well with our former XRD analysis. Figure S3C in the Supporting Information shows a high-resolution spectrum of Ni 2p. Note

dx.doi.org/10.1021/am400055a | ACS Appl. Mater. Interfaces 2013, 5, 2634−2640

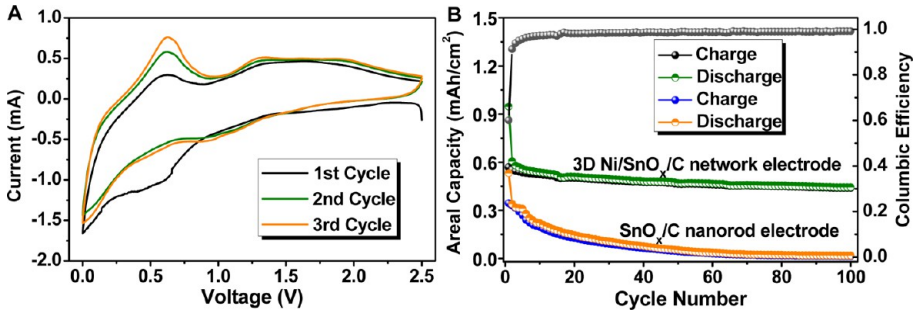

Figure 4. (A) Cyclic voltammetry curves of the 3D Ni/SnO_x/C network electrode for the first few cycles in the potential range of 0.0−2.5 V at a scan rate of 0.5 mV/s. (B) Areal Charge/discharge capacity of 3D Ni/SnO_x/C network and SnO_x/C nanorod electrodes at current rates of 0.4 mA/cm^2 for 100 cycles.

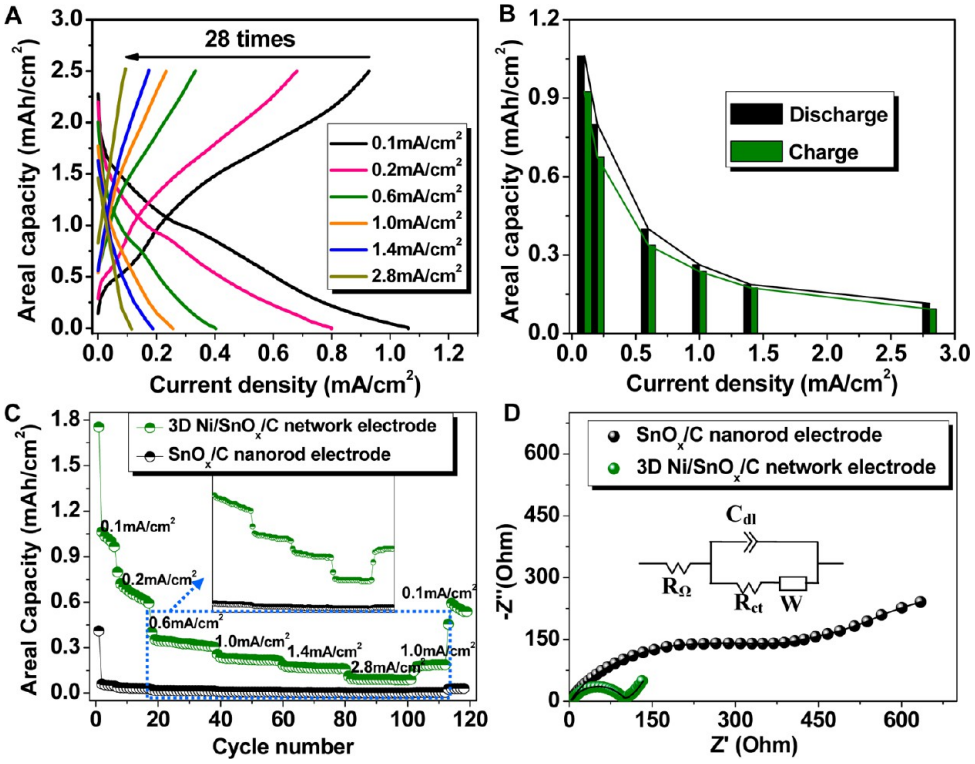

Figure 5. Rate capability of 3D Ni/SnO_x/C electrode. (A) Galvastatic profiles recorded at 0.1, 0.2, 0.6, 1.0, 1.4, and 2.8 mA/cm^2. (B) Areal capacity vs current density curve and (C) Areal discharge capacity at various current rates (from 0.1−2.8 mA/cm^2) in comparison with that of the SnO_x/C nanorod electrode. Inset is the enlarged image of the profile in the dotted line box. (D) Nyquist plots of the 3D Ni/SnO_x/C network (circles) and conventional SnO_x/C nanorod (rectangles) electrodes and fitting results (line) using the equivalent circuit shown in the inset.

that two weak peaks are centered at the binding energy of 855.5 and 873.2 eV with a spin energy separation of 17.7 eV, which correspond to the Ni $2p_{3/2}$ and Ni $2p_{1/2}$, respectively. Also, a satellite peak emerges at 861.6 eV, which might be ascribed to the partial oxidation of Ni nanowalls in the air atmosphere.[28] On the basis of the total XPS and XRD analysis, it is evidenced that our products possess an interesting Ni/SnO_x/C hybrid nature.

To investigate their electrochemical performances, the as-prepared 3D Ni/SnO_x/C hybrid nanostructured arrays and SnO_x/C nanorod arrays on substrate were assembled directly as anode for LIMBs, saving the tedious procedures for making electrodes. Figure 4A shows the typical cyclic voltammetry (CV) curves of the 3D Ni/SnO_x/C electrode over the potential window of 0−2.5 V at a scan rate of 0.5 mV/s for the first three cycles. In the first cathodic sweep, a broad irreversible reduction peak was centered at 0.7 V, which could be ascribed to the formation of solid-state electrolyte interface (SEI) film and the irreversible reduction of SnO_2 to Sn.[27−29] During the anodic sweep, one oxidation peak appeared at 0.6 V, corresponding to the dealloying reaction of Li−Sn alloys.[17,29−31] Another oxidation peak located at ∼1.3 V was also detected, which could be assigned to the partially reversible reaction of SEI layer formation as well as the slight oxidation of Sn during the charge/discharge process. The areal capacity and cycling performances of Ni/SnO_x/C and SnO_x/C hybrid electrodes were evaluated by galvanostatic discharge−charge measurements at a current density of 0.4 mA/cm^2 (Figure 4B). It is noteworthy that the initial discharge areal capacity of 3D Ni/SnO_x/C hybrid electrode was ∼0.95 mA h/cm^2 (equivalent to a specific capacity of ∼1187.5 mA h/g, as shown inFigure S4 in the Supporting Information), which is much larger than that of SnO_x/C on 2D planar electrode with a capacity of only 0.53 mA h/cm^2. Particularly, the areal capacities of the 3D Ni/

SnO_x/C electrode were always higher than those of SnO_x/C nanorod electrode in the whole cycling testing. The 3D Ni/SnO_x/C network exhibited a much better capacity retention capability, capable of delivering a high reversible areal capacity of 0.47 mA h/cm^2 (~587.5 mA h/g) after 50 cycles (with a 77.5% reversible capacity retention), whereas for the case of SnO_x/C nanorod electrode, a poor capacity of only 0.045 mA h/cm^2 was retained (the reversible capacity retention is only around 8%) after going through 50 charge−discharge cycles. Even after 100 cycles, the Ni/SnO_x/C hybrid nanostructured arrays still retained a capacity of ~0.44 mA h/cm^2 (~550 mA h/g, retaining 72% reversible capacity), and the Coulombic efficiencies were calculated nearly close to 100% during the most cycles. To understand the better cycling behavior of the 3D Ni/SnO_x/C hybrid electrode, the morphology and structural changes of cycled electrodes were further examined by SEM (see Figure S5A, B in the Supporting Information). It is noted that after 100 cycles charge/discharge between 0 and 2.5 V at a current rate of 0.4 mA/cm^2, we still find the trace of the original Ni network structures, although the grown SnO_x nanorods became aggregated or crumbled.

Rate performances of 3D Ni/SnO_x/C hybrid nanostructured arrays and 2D SnO_x/C nanorod electrodes are also evaluated. Figure 5A shows voltage profiles of 3D Ni/SnO_x/C electrodes tested at various current densities. The relationship between the areal capacity vs current density is depicted in Figure 5B. At a low current rate of 0.1 mA/cm^2, the 3D Ni/SnO_x/C hybrid electrode can deliver a reversible areal capacity of ~1.06 mA h/cm^2. Upon the increase in current rates, the electrode of Ni/SnO_x/C shows reversible areal capacities of 0.80 mAh/cm^2 (0.2 mA/cm^2), 0.40 mAh/cm^2 (0.6 mA/cm^2), 0.26 mA h/cm^2 (1.0 mA/cm^2) and 0.19 mAh/cm^2 (1.4 mA/cm^2), respectively. Even at a high rate up to 2.8 mA/cm^2 (~28 times that of 0.1 mA/cm^2), the Ni/SnO_x/C hybrid electrode still maintains a capacity of 0.11 mA h/cm^2 (charged/discharged in 33 s). While for the SnO_x/C nanorod electrode (Figure 5C), the areal capacity quickly drops to near zero (~0.006 mA h/cm^2) as the current rate merely increased up to ~1.0 mA/cm^2. To gain further insight into their difference, we carried out electrochemical impedance spectroscopy (EIS) measurements to identify the relationship between the electrochemical performance and electrode kinetics. Corresponding Nyquist plots are presented in Figure 5D. On the basis of the modified Randles equivalent circuit given in the inset of Figure 5D, the 3D Ni/SnO_x/C electrode shows a much lower charge-transfer resistance (R_{ct}) than that of 2D SnO_x/C electrode (95.7 vs 229 Ω). This indicates that the 3D-designed electrode with Ni frameworks inside has a smaller ionic resistance and enhanced kinetics.[32]

Compared with the planar thin-film electrode of SnO_x/C nanorods, the Ni/SnO_x/C electrode with a 3D hierarchical architecture exhibits superior lithium-storage capacity and cycling stability. We believe that the formed 3D hybrid nanostructured arrays play a key role to improve the electrochemical performances for LIMBs, which is thought based on the following reasons. First and foremost, the use of 3D architectured electrode can greatly promote the mass loading of active materials per unit area. Accordingly, there are more reaction sites available for Li^+ insertion/extraction, and thus the areal capacity of the electrode can be significantly enhanced. Second, the inner nanostructured Ni current collectors can provide both the superhighway for electron transport and effective path for Li^+ diffusion, guaranteeing the good rate performance of the Ni/SnO_x/C electrode. Last, the sufficient void spaces existing in networks could help to accommodate the volume changes as well as mitigate the associated strain to some extent upon repeated lithium insertion/extraction. Besides, the 3D Ni network structure could also aid to the uniform dispersion of loaded SnO_x active materials into the conductive matrix, eventually decreasing the aggregation rate of SnO_x and prolonging the cycling lifetime of LIMBs.

CONCLUSIONS

In summary, we have designed and fabricated the 3D Ni/SnO_x/C hybrid nanostructured arrays through a simple hydrothermal followed by a calcination-reduction process. The 3D hierarchical hybrid nanostructured arrays were used as binder-free anodes for LIMBs, demonstrating a much higher areal capacity of 0.95 mA h/cm^2 at the first cycle than that of SnO_x/C nanorods on planar electrode at 0.4 mA/cm^2 current rate. The 3D Ni/SnO_x/C hybrid electrode also exhibits good rate capability, with 0.11 mA h/cm^2 areal capacity retained even when rapidly charged in 33 s at a large current rate of 2.8 mA/cm^2. Using the unique 3D architectured electrode, involving the inner Ni conducting matrix and the outer SnO_x/C hybrid arrays, can effectively enhance the capacity per unit area by the increase of active materials loading as well as reaction sites, facilitate electron transfer from active materials to current collectors, and help to alleviate large volume changes during cycling. What's more, this novel 3D hybrid network design could be extended to a variety of other energy conversion and storage fields, which holds great promise in realizing more applications that can not be readily achieved without a 3D design.

ASSOCIATED CONTENT

Supporting Information

XRD result and SEM observations of pristine SnO_2 and SnO_x/C nanorod arrays; XPS spectrum and cycling behaviors of Ni/SnO_x/C hybrid nanostructured arrays; SEM observation toward the cycled electrode. This information is available free of charge via the Internet at http://pubs.acs.org/.

AUTHOR INFORMATION

Corresponding Author

*E-mail: jhzhu@phy.ccnu.edu.cn (J.Z.); xthuang@phy.ccnu.edu.cn (X.H.). Phone: 86-027-67861185. Fax: 86-027-67861185.

Notes

The authors declare no competing financial interest.

ACKNOWLEDGMENTS

This work is supported by the National Natural Science Foundation of China (51170285, 51102105) and the Natural Science Foundation of Hubei Province (2011CDB154). The authors thank the Center for Electron Microscopy at Wuhan University for the HRTEM observations.

REFERENCES

(1) Yang, S. B.; Feng, X. L.; Ivanovici, S.; Müllen, K. *Angew. Chem., Int. Ed.* **2010**, *49*, 8408.

(2) Luo, Y. S.; Luo, J. S.; Jiang, J.; Zhou, W. W.; Yang, H. P.; Qi, X. Y.; Zhang, H.; Fan, H. J.; Yu, Y.W. Denis; Li, C. M.; Yu, T. *Energy Environ. Sci.* **2012**, *5*, 6559.

(3) Shaijumon, M. M.; Perre, E.; Daffos, B.; Taberna, P.-L.; Tarascon, J.-M.; Simon, P. *Adv. Mater.* **2010**, *22*, 4978.

(4) Chen, J. S.; Zhu, T.; Yang, X. H.; Yang, H. G.; Lou, X. W. *J. Am. Chem. Soc.* **2010**, *132*, 13162.
(5) Guan, C.; Li, X. L.; Wang, Z. L.; Cao, X. H.; Soci, C.; Zhang, H.; Fan, H. J. *Adv. Mater.* **2012**, *24*, 4186.
(6) Liu, B.; Zhang, J.; Wang, X. F.; Chen, G.; Chen, D.; Zhou, C. W.; Shen, G. Z. *Nano Lett.* **2012**, *12*, 3005.
(7) Hu, L. B.; Wu, H.; Gao, Y. F.; Cao, A. Y.; Li, H. B.; McDough, J.; Xie, X.; Zhou, M.; Cui, Y. *Adv. Energy Mater.* **2011**, *1*, 523.
(8) (a) Jiang, J.; Li, Y. Y.; Liu, J. P.; Huang, X. T.; Yuan, C. Z.; Lou, X. W. *Adv. Mater.* **2012**, *24*, 5166. (b) Jiang, J.; Zhu, J. H.; Feng, Y. M.; Liu, J. P.; Huang, X. T. *Chem. Commun.* **2012**, *48*, 7471.
(9) Ji, H. X.; Zhang, L. L.; Pettes, M. T.; Li, H. F.; Chen, S. S.; Shi, L.; Piner, R.; Ruoff, R. S. *Nano Lett.* **2012**, *12*, 2446.
(10) Ge, M. Y.; Rong, J. P.; Fang, X.; Zhou, C. W. *Nano Lett.* **2012**, *12*, 2318.
(11) Zhang, H. G.; Braun, P. V. *Nano Lett.* **2012**, *12*, 2778.
(12) Evanoff, K.; Khan, J.; Balandin, A. A.; Magasinski, A.; Ready, W. J.; Fuller, T. F.; Yushin, G. *Adv. Mater.* **2012**, *24*, 533.
(13) Yu, Y.; Gu, L.; Lang, X. Y.; Zhu, C. B.; Fujita, T.; Chen, M. W.; Maier, J. *Adv. Mater.* **2011**, *23*, 2443.
(14) Wang, W.; Tian, M.; Abdulagatov, A.; George, S. M.; Lee, Y.-C.; Yang, R. G. *Nano Lett.* **2012**, *12*, 655.
(15) Wang, Z. Y.; Zhou, L.; Lou, X. W. *Adv. Mater.* **2012**, *24*, 1773.
(16) Derrien, G.; Hassoun, J.; Panero, S.; Scrosati, B. *Adv. Mater.* **2007**, *19*, 2336.
(17) Park, M.-S.; Kang, Y.-M.; Wang, G.-X.; Dou, S.-X.; Liu, H.-K. *Adv. Funct. Mater.* **2008**, *18*, 455.
(18) Wang, J. Z.; Du, N.; Zhang, H.; Yu, J. X.; Yang, D. R. *J. Phys. Chem. C* **2011**, *15*, 11302.
(19) Lou, X. W.; Chen, J. S.; Chen, P.; Archer, L. A. *Chem. Mater.* **2009**, *21*, 2868.
(20) Wang, Z. Y.; Wang, Z. C.; Madhavi, S.; Lou, X. W. *Chem.—Eur. J.* **2012**, *18*, 7561.
(21) Zhou, W. W.; Cheng, C. W.; Liu, J. P.; Tay, Y. Y.; Jiang, J.; Jia, X. T.; Zhang, J. X.; Gong, H.; Hng, H. H.; Yu, T.; Fang, H. J. *Adv. Funct. Mater.* **2011**, *21*, 2439.
(22) (a) Liu, J. P.; Li, Y. Y.; Huang, X. T.; Ding, R. M.; Hu, Y. Y.; Jiang, J.; Liao, L. *J. Mater. Chem.* **2009**, *19*, 1859. (b) Zhang, S. C.; Xing, L. L.; Jiang, T.; Du, Z. J.; Li, F.; Liu, W. B. *J. Power Sources* **2011**, *196*, 6915.
(23) (a) Jiang, J.; Li, Y. Y.; Liu, J. P.; Huang, X. T. *Nanoscale* **2011**, *3*, 45. (b) Liu, J. P.; Li, Y. Y.; Ding, R. M.; Jiang, J.; Hu, Y. Y.; Ji, X. X.; Chi, Q. B.; Zhu, Z. H.; Huang, X. T. *J. Phys. Chem. C* **2009**, *113*, 5336. (c) Jiang, J.; Zhu, J. H.; Ding, R. M.; Li, Y. Y.; Wu, F.; Liu, J. P.; Huang, X. T. *J. Mater. Chem.* **2011**, *21*, 15969.
(24) Zhu, J. H.; Jiang, J.; Liu, J. P.; Ding, R. M.; Ding, H.; Feng, Y. M.; Wei, G. M.; Huang, X. T. *J. Solid State Chem.* **2011**, *184*, 578.
(25) Zhang, D. F.; Sun, L.-D.; Jia, C.-J.; Yan, Z.-G.; You, L.-P.; Yan, C.-H. *J. Am. Chem. Soc.* **2005**, *127*, 13492.
(26) (a) Jiang, J.; Liu, J. P.; Zhou, W. W.; Zhu, J. H.; Huang, X. T.; Qi, X. Y.; Zhang, H.; Yu, T. *Energy Environ. Sci.* **2011**, *4*, 5000. (b) Zhu, J. H.; Jiang, J.; Liu, J. P.; Ding, R. M.; Li, Y. Y.; Feng, Y. M.; Wei, G. M.; Huang, X. T. *RSC Adv.* **2011**, *1*, 1020.
(27) Du, N.; Zhang, H.; Chen, B. D.; Ma, X. Y.; Yang, D. R. *Chem. Commum.* **2008**, 3028.
(28) Ding, H.; Zhu, J. H.; Jiang, J.; Ding, R. M.; Feng, Y. M.; Wei, G. M.; Huang, X. T. *RSC Adv.* **2012**, *2*, 10324.
(29) Chen, J. S.; Chean, Y. L.; Chen, Y. T.; Jayaprakash, N.; Madhavi, S.; Yang, Y. H.; Lou, X. W. *J. Phys. Chem. C* **2009**, *113*, 20504.
(30) Yin, X. M.; Li, C. C.; Zhang, M.; Hao, Q. Y.; Liu, S.; Chen, L. B.; Wang, T. H. *J. Phys. Chem. C* **2010**, *114*, 8084.
(31) Xu, C. H.; Sun, J.; Gao, L. *J. Mater. Chem.* **2012**, *22*, 975.
(32) (a) Wang, Y. G.; Hong, Z. S.; Wei, M. D.; Xia, Y. G. *Adv. Funct. Mater.* **2012**, *22*, 5185. (b) Zhu, H.; Wang, X. L.; Liu, X. X.; Yang, X. R. *Adv. Mater.* **2012**, *24*, 6524.